Atmospheric
Measurement
Techniques
Discussions

Open Access

EGU

1 POMINO-GEMS : A Research Product for Tropospheric NO₂ Columns from

2 Geostationary Environment Monitoring Spectrometer

3 Yuhang Zhang[1], Jintai Lin[1], Jhoon Kim[2], Hanlim Lee[3], Junsung Park[3], Hyunkee Hong[4], Michel Van

4 Roozendael[5], Francois Hendrick[5], Ting Wang[6,7], Pucai Wang[6,7], Qin He[8], Kai Qin[8], Yongjoo Choi[9],

5 Yugo Kanaya[10], Jin Xu[11], Pinhua Xie[7,11], Xin Tian[12], Sanbao Zhang[13], Shanshan Wang[13], Robert

6 Spurr[14], Lulu Chen[15], Hao Kong[1], Mengyao Liu[16]

7 [1]Laboratory for Climate and Ocean-Atmosphere Studies, Department of Atmospheric and Oceanic

8 Sciences, School of Physics, Peking University, Beijing, 100871, China

9 [2]Department of Atmospheric Sciences, Yonsei University, Seoul, South Korea

10 [3]Pukyong National University, Busan, South Korea

11 [4]National Institute of Environmental Research, Incheon, South Korea

12 [5]BIRA-IASB, Belgian Institute for Space Aeronomy, Brussels, Belgium

13 [6]CNRC & LAGEO, Institute of Atmospheric Physics, Chinese Academy of Sciences, Beijing, 100029,

14 China

15 [7]University of Chinese Academy of Sciences, Beijing, 100049, China

16 [8]School of Environment and Geoinformatics, China University of Mining and Technology, Xuzhou,

17 Jiangsu, 221116, China

18 [9]Department of Environmental Science, Hankuk University of Foreign Studies, Yongin, South Korea

19 [10]Research Institute for Global Change, Japan Agency for Marine-Earth Science and Technology

20 (JAMSTEC), Yokohama, 2360001, Japan

21 [11]Key Laboratory of Environmental Optics and Technology, Anhui Institute of Optics and Fine

22 Mechanics, Chinese Academy of Science, Hefei, 230031, China

23 [12]Information Materials and Intelligent Sensing Laboratory of Anhui Province, Institutes of Physical

24 Science and Information Technology, Anhui University, Hefei, Anhui, 230601, China

25 [13]Shanghai Key Laboratory of Atmospheric Particle Pollution and Prevention (LAP3), Department of

26 Environmental Science and Engineering, Fudan University, Shanghai, 200433, China

27 [14]RT Solutions Inc., Cambridge, Massachusetts, 02138, USA

28 [15]College of Urban and Environmental Sciences, Peking University, Beijing, 100871, China

29 [16]R&D Satellite Observations Department, Royal Netherlands Meteorological Institute, De Bilt, the

30 Netherlands

31 *Correspondence to*: Jintai Lin (linjt@pku.edu.cn)

32 **Abstract**

33   Nitrogen dioxide (NO_2) is a major air pollutant. Tropospheric NO_2 vertical column densities (VCDs)

34 retrieved from sun-synchronous satellite instruments have provided abundant NO_2 data for

35 environmental studies, but such data are limited by insufficient temporal sampling (e.g., once a day). The

36 Geostationary Environment Monitoring Spectrometer (GEMS) launched in February 2020 monitors NO_2

37 at an unprecedented high temporal resolution. Here we present a research product for tropospheric NO_2

38 VCDs, referred to as POMINO-GEMS. We develop a hybrid retrieval method combining GEMS and

39 TROPOMI observations as well as GEOS-Chem simulations to generate hourly tropospheric NO_2 slant

40 column densities (SCDs). We then derive tropospheric NO_2 air mass factors (AMFs) with explicit

41 corrections for the anisotropy of surface reflectance and aerosol optical effects, through pixel-by-pixel

42 radiative transfer calculations. Prerequisite cloud parameters are retrieved with the O_2-O_2 algorithm by

43 using ancillary parameters consistent with those used in NO_2 AMF calculations. Initial retrieval of

44 POMINO-GEMS tropospheric NO_2 VCDs for June–August 2021 reveals strong hotspot signals over

45 megacities and distinctive diurnal variations over polluted and clean areas. POMINO-GEMS NO_2 VCDs

46 agree well with our POMINO-TROPOMI v1.2.2 product ($R = 0.97$, and NMB = 3.6%) over Asia.

47 Comparison with ground-based MAX-DOAS VCD data at nine sites shows a small bias of POMINO-

48 GEMS (NMB = –15.7%); however, the correlation for diurnal variation varies from -0.66 to 0.90,

49 suggesting location-dependent performance. Surface NO_2 concentrations estimated from POMINO-

50 GEMS VCDs are consistent with measurements from the Ministry of Ecology and Environment of China

51 at 855 sites (NMB = –24.1%, and $R = 0.95$ for diurnal correlation averaged over all sites). POMINO-

52 GEMS data will be made freely available for users to study the spatiotemporal variations, sources and

53 impacts of NO_2.

54 **1. Introduction**

55   Tropospheric nitrogen dioxide (NO_2) is an important air pollutant. It is a threat to human health, and

56 also contributes to the formation of tropospheric ozone (O_3) and nitrate aerosol as an essential precursor

57 (Crutzen, 1970; Shindell et al., 2009; Hoek et al., 2013; Chen et al., 2022). Satellite instruments provide

58 observations of tropospheric NO_2 on a global scale, and they have been extensively used to estimate

59 emissions of nitrogen oxides (NOx = NO + NO_2) (Lin and Mcelroy, 2011; Beirle et al., 2011; Gu et al.,

60 2014; Kong et al., 2022a), surface NO_2 concentrations (Wei et al., 2022; Cooper et al., 2022), trends and

61 variabilities (Richter et al., 2005; Cui et al., 2016; Krotkov et al., 2016; Van Der A et al., 2017), and

62 impacts on human health and environment (Chen et al., 2021).

63   To date, most spaceborne instruments for NO_2 measurements, including the Ozone Monitoring

64 Instrument (OMI), the Global Ozone Monitoring Experiment 2 (GOME-2) and the TROPospheric

65 Monitoring Instrument (TROPOMI), are mounted on sun-synchronous low Earth orbit (LEO) satellites

66 (Boersma et al., 2011; Richter et al., 2011; Van Geffen et al., 2020). These instruments passively measure

67   backscattered radiance from the Earth's atmosphere, and measurements at each ground location are done

68   1–2 times a day. The Geostationary Environment Monitoring Spectrometer (GEMS) on board the

69   Geostationary Korea Multi-Purpose Satellite-2B (GK-2B) was successfully launched in February 2020.

70   The instrument provides measurements of NO_2 and other pollutants in the daytime on an hourly basis

71   (Kim et al., 2020). It complements LEO satellite observations by providing a more comprehensive

72   picture of the daytime evolution of NO_2.

73   There are three successive stages in the retrieval of tropospheric NO_2 vertical column densities

74   (VCDs) in the UV-Vis range based on satellite observations. The first step is to retrieve total NO_2 slant

75   column densities (SCDs) with the Differential Optical Absorption Spectroscopy (DOAS) technique,

76   which provides the abundance of NO_2 along the effective light path from the sun through the atmosphere

77   to the satellite instrument. Next, the contributions from stratospheric NO_2 to the total SCDs are removed

78   in order to obtain tropospheric NO_2 SCDs. Finally, the tropospheric SCDs are converted to VCDs using

79   calculated air mass factors (AMFs), which are highly sensitive to the observation geometry, cloud

80   parameters, aerosols, surface conditions and the shape of the NO_2 vertical distribution. Over polluted

81   areas, errors in the retrieved tropospheric NO_2 VCDs are dominated by the uncertainties in AMF

82   calculations (Boersma et al., 2004; Lorente et al., 2016); errors are sensitive to assumptions on aerosol

83   optical effects, surface reflectance, and a priori NO_2 vertical profiles (Zhou et al., 2010; Lin et al., 2014;

84   Lin et al., 2015; Vasilkov et al., 2016; Lorente et al., 2018; Liu et al., 2019; Liu et al., 2020; Vasilkov et

85   al., 2021).

86   The official GEMS retrieval algorithm for tropospheric NO_2 VCDs is developed by Lee et al. (2020).

87   The total NO_2 SCDs are retrieved using the DOAS technique; they are then converted to total NO_2 VCDs

88   by using the AMFs calculated based on the linearized pseudo-spherical scalar and vector discrete ordinate

89   radiative transfer code (VLIDORT). Finally, stratosphere-troposphere separation (STS) is performed to

90   derive tropospheric NO_2. Validation results have shown the overall capability of the official GEMS NO_2

91   algorithm, but several problems are also reported, such as overestimation of total NO_2 SCDs and

92   tropospheric NO_2 VCDs, and some degree of striping in NO_2 retrieval data.

93   In this study, we present a research product which we name as POMINO-GEMS. This product is

94   built upon our POMINO algorithm which focuses on the tropospheric AMF calculations and has been

95   applied to OMI and TROPOMI (Lin et al., 2014; Lin et al., 2015; Liu et al., 2019; Liu et al., 2020; Zhang

Atmospheric
Measurement
Techniques
Discussions

Open Access

EGU

96   et al., 2022). Here we extend the AMF calculation by constructing a hybrid method to estimate

97   tropospheric SCDs for GEMS. The hybrid method makes use of the total SCDs from the official GEMS

98   product, total SCDs and stratospheric VCDs from the official TROPOMI product, as well as hourly

99   variations of stratospheric VCDs from GEOS-Chem simulations. We validate our initial set of retrieval

100   results for tropospheric NO_2 VCDs in June-July-August (JJA) 2021 by using independent data of

101   tropospheric NO_2 from the POMINO-TROPOMI v1.2.2 product, ground-based MAX-DOAS

102   measurements, and surface concentration observations from the Ministry of Ecology and Environment

103   (MEE) of China. We provide a simplified estimate of retrieval errors in the end.

104   **2. Method and data**

105   **2.1 Construction of POMINO-GEMS retrieval algorithm**

106   Figure 1 shows the flow chart of POMINO-GEMS retrieval algorithm. There are two essential steps.

107   The first is to calculate tropospheric NO_2 SCDs on an hourly basis, through fusion of total SCDs from

108   the official GEMS v1.0 L2 NO_2 product, total SCDs and stratospheric VCDs from the TROPOMI PAL

109   v2.3.1 L2 NO_2 product, and diurnal variations of stratospheric NO_2 from nested GEOS-Chem (v9-02)

110   simulations. We then calculate tropospheric NO_2 AMFs to convert SCDs to VCDs. Details are described

111   in the next sub-sections.
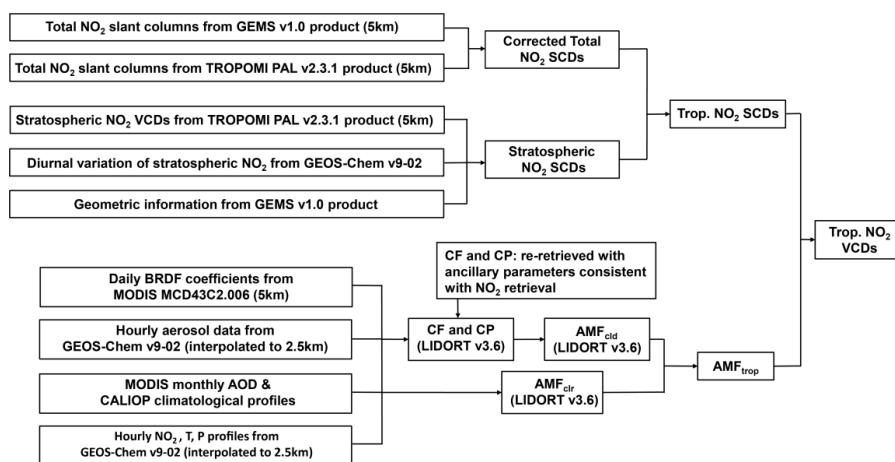
112

113   **Figure 1. Flow chart of POMINO-GEMS retrieval algorithm. The numbers in the boxes, such as 5 km, refer**

114   **to horizontal resolutions.**

115   **2.1.1 GEMS NO_2 and cloud data**

116   The GEMS instrument is on board the GK-2B satellite locating at 128.2°E over the equator (Kim

117   et al., 2020). The spectral wavelength range of GEMS is 300-500 nm, covering main absorption spectra

118   of aerosols and trace gases. The nominal spatial resolution is typically 7 km × 8 km for gases and 3.5 km

119   × 8 km for aerosols in the eastern and central scan domain; however, the north-south spatial resolution

120   can exceed 25 km in the western side. The whole field of view (FOV) covers about 20 Asian countries

121   within latitudes 5°S to 45°N and longitudes 80°E to 152°E. Given the variation of solar zenith angle

122   (SZA), there are four scan scenarios, including Half East (HE), Half Korea (HK), Full Central (FC) and

123   Full West (FW), moving from east to west. It takes 30 minutes (for example, 00:45–01:15 UTC) for

124   GEMS to scan its full coverage during each measurement, and the next 30 minutes to transmit data to

125   the ground data center. The number of hourly GEMS observations per day varies from 6 in winter to 10

126   in summer, corresponding to the annual movement of subsolar points relative to the Earth.

127   We take hourly total NO_2 SCDs from the official GEMS v1.0 L2 NO_2 product, and convert them to

128    $0.05° \times 0.05°$ gridded data by means of an area-weighted oversampling technique. We also use continuum

129   reflectances and O_2-O_2 SCDs from the official GEMS v1.0 L2 cloud product to re-calculate cloud

130   parameters as a prerequisite for tropospheric NO_2 AMF calculations. Details of the GEMS retrievals can

131   be found in the algorithm theoretical basis document (ATBD) (Lee et al., 2020).

2.1.2 TROPOMI NO_2 data

133   The TROPOMI instrument is on board the sun-synchronous satellite Sentinel-5 Precursor, with an

134   Equator overpass time of about 13:30 local solar time (LST) (Van Geffen et al., 2020). It provides

135   measurements for various trace gases, aerosols and cloud properties with a wide spectral range from UV

136   to shortwave infrared. TROPOMI achieves daily global coverage with a full swath width of about 2600

137   km. The horizontal resolution is 3.5 km × 7 km (3.5 km × 5.5 km since 6 August 2019) at nadir, with a

138   maximum width of about 14 km for pixels near the edge of the swath.

139   We use total NO_2 SCDs and stratospheric NO_2 VCDs from the official TROPOMI PAL v2.3.1 L2

140   NO_2 product, and convert them to $0.05° \times 0.05°$ gridded data, again using an area-weighted oversampling

141   technique. Details of TROPOMI total SCD retrievals and stratospheric VCD calculations are given in

142   the TROPOMI ATBD (Van Geffen et al., 2022a). This intermediate product is reprocessed with

143   TROPOMI NO_2 data processor v2.3.1 for the period from 1 May 2018 to 14 November 2021; it will be

144   replaced by the full mission reprocessing with NO_2 processor v2.4.0 in the future (Eskes et al., 2021).

145   The most important improvement in this product over the previous OFFL v1.3 is the replacement of the

146   FRESCO-S algorithm with the FRESCO-wide cloud retrieval algorithm, which leads to more reasonable

147   cloud pressure (CP) estimates and substantial increases in tropospheric NO_2 VCDs (by 20%–50%) over

148   polluted regions like Eastern China in winter (Eskes et al., 2021; Van Geffen et al., 2022b).

149   In addition, we use the POMINO-TROPOMI v1.2.2 tropospheric NO_2 VCD product to compare

150   with POMINO-GEMS results. The previous POMINO-TROPOMI v1 data show better data in polluted

151   situations and improved consistency with MAX-DOAS measurements when compared with the official

152   TM5-MP-DOMINO (OFFLINE) product (Liu et al., 2020). POMINO-TROPOMI v1.2.2 improves upon

153   v1 by (1) using tropospheric NO_2 SCD and CP data from the updated TROPOMI PAL v2.3.1 NO_2 product,

154   (2) interpolating the daily NO_2, pressure, temperature and aerosol vertical profiles into a horizontal grid

155   of 2.5 km x 2.5 km for subsequent tropospheric AMF calculations, and (3) including several minor bug

156   fixes.

2.1.3 Calculation of total NO_2 SCDs

158   We use TROPOMI data to correct GEMS total NO_2 SCDs, taking into account potential issues in

159   GEMS data. Figures 2a and b show the spatial distribution of monthly mean total NO_2 geometric column

160   densities (GCDs, calculated as SCDs divided by geometric AMFs) in June 2021 from TROPOMI PAL

161   v2.3.1 and GEMS v1.0, respectively. The horizontal resolution is $0.05° \times 0.05°$. The GCDs are used to

162   compare the two products after removing the effect of measurement geometry. Matching for each day

163   between hourly GEMS observations and the TROPOMI data at the closest observation time is done to

164   ensure temporal compatibility. The figures show that the spatial pattern of GEMS GCDs agrees well with

165   that from TROPOMI, with high values over the North China Plain (NCP) and Northwestern India, as

166   well as major metropolitan clusters such as Seoul and the Yangtze River Delta (YRD). However, there

167   are two systematic problems in GEMS GCDs. Firstly, the GEMS GCD values are abnormally high over

168   the northern and northwestern part of GEMS FOV, especially over Mongolia, Qinghai, Inner Mongolia,

169   Xinjiang and Tibet of China. Secondly, the west-east stripes exist over the whole domain, similar to the

170   spurious across-track variability issue for OMI. This stripe issue is likely associated with the specific

171   scan modes of GEMS, as well as periodically occurring bad pixels as one of remaining calibration issues

172   (Boersma et al., 2011; Lee et al., 2023).

Atmospheric
Measurement
Techniques
Discussions
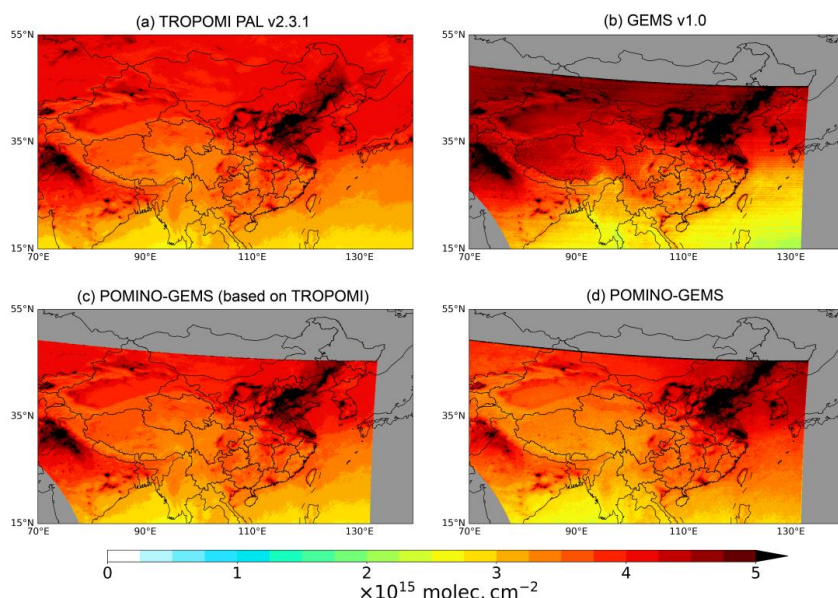
Figure 2. Spatial distribution of monthly mean total NO₂ GCDs on a 0.05° × 0.05 ° grid in June 2021. (a) TROPOMI PAL v2.3.1 product, (b) official GEMS v1.0 product, (c) corrected POMINO-GEMS product that spatiotemporally match with TROPOMI, and (d) corrected POMINO-GEMS product at all observation hours.

To correct the two issues in the GEMS official total NO₂ SCD product, we combine GEMS and TROPOMI observations to obtain hourly 0.05° × 0.05 °corrected total NO₂ SCDs for each day using Eqs. (1) and (2):

$$\Delta\text{GCD} = \frac{1}{n}\sum_{i=1}^{n}(\text{GCD}_{\text{total},h_i}^{\text{TROPOMI}} - \text{GCD}_{\text{total},h_i}^{\text{GEMS}})\qquad(1)$$

$$\text{SCD}_{\text{total},h}^{\text{corrected}} = \text{SCD}_{\text{total},h}^{\text{GEMS}} + \Delta\text{GCD} \times \text{AMFgeo}_h^{\text{GEMS}}\qquad(2)$$

In Eqs. (1) and (2), index h represents the hour of GEMS observations on each day; h_i the hour when both GEMS and TROPOMI have valid observations for the same grid cell; and n the number of h_i. The value of n is 1 or 2 depending on the overpass times of TROPOMI. There are two steps in the correction process. Firstly, we calculate a geometry-independent correction map for each day using total NO₂ GCDs from GEMS and TROPOMI that match spatially and temporally (Eq. (1)). We use the absolute difference instead of a scaling factor as a simple correction. We then apply the correction to the original GEMS total NO₂ SCDs at each hour on the same day, by accounting for the diurnal variation in AMF associated with measurement geometry (Eq. (2)).

Atmospheric
Measurement
Techniques
Discussions

Open Access

EGU

191   Figure 2c shows monthly mean corrected POMINO-GEMS total NO_2 GCDs in June 2021 after

192   spatial and temporal matching with TROPOMI. The corrected GCD values in northern GEMS FOV are

193   much reduced compared with those in the original GEMS data. Moreover, most stripe-like patterns are

194   removed in the corrected GCDs.

195   Figure 2d is similar to Fig. 2c but for GCDs averaged at all observation hours in June 2021. The

196   differences between Figures 2c and 2d indicate the influence of different sampling times as well as the

197   limitation of daily correction map. Specifically, the correction value of each grid cell is calculated at the

198   specific hour when both GEMS and TROPOMI have valid observations, but this value is applied to

199   original GEMS SCDs at all hours.

200   **2.1.4 Calculation of stratospheric and tropospheric NO_2 SCDs**

201   We construct a dataset of hourly stratospheric NO_2 SCDs at $0.05° \times 0.05°$ by using TROPOMI

202   stratospheric NO_2 VCDs, diurnal variation of stratospheric NO_2 VCDs provided by GEOS-Chem

203   simulations, and GEMS geometric AMFs. Nested GEOS-Chem v9-02 simulations for Asia at 0.25° lat.

204    $\times 0.3125°$ long. with 47 vertical layers are driven with daily GEOS-FP meteorological fields; see details

205   in our previous studies (Lin et al., 2014; Lin et al., 2015). We add the simulated NO_2 sub-columns within

206   layers 37 to 43 (roughly above 17 km) to represent NO_2 VCDs in the stratosphere.

207   First, we calculate stratospheric NO_2 VCDs at a reference hour for each day using Eqs. (3) and (4):

208
$$\text{ratio}_{h_0}^h = \frac{\text{VCD}_{\text{strat},h}^{\text{GC}}}{\text{VCD}_{\text{strat},h_0}^{\text{GC}}} \tag{3}$$

209
$$\text{VCD}_{\text{strat},h_0} = \frac{1}{n}\sum_{i=1}^{n}\frac{\text{VCD}_{\text{strat},h_i}^{\text{TROPOMI}}}{\text{ratio}_{h_0}^{h_i}} \tag{4}$$

210   Here, Eq. (3) defines the ratio of GEOS-Chem simulated stratospheric NO_2 at hour h to that at the

211   reference hour h_0, which is chosen to be 00:00 UTC (Figure S1). In Eq. (4), h_i represents the observation

212   time of every TROPOMI orbit that overlaps with GEMS FOV, and n the number of h_i for each grid cell.

213   Second, we use the ratio from a given time h to h_0 and stratospheric NO_2 VCDs at h_0 to derive

214   stratospheric NO_2 VCDs at h for each day (Eq. (5)).

215
$$\text{VCD}_{\text{strat},h} = \text{VCD}_{\text{strat},h_0} \times \text{ratio}_{h_0}^h \tag{5}$$

216   Figure 3 shows the derived monthly mean stratospheric NO_2 VCDs at each hour in June 2021 on a 0.05°

217    $\times 0.05°$ grid. The spatial patterns are very similar at different times, indicating weak simulated diurnal

218   variation of stratospheric NO_2 in summer. There is a strong meridional gradient of stratospheric NO_2,

219   with the higher values in the north associated with longer lifetimes.

220   Finally, we use GEMS geometric AMFs to convert the stratospheric NO$_2$ VCDs to SCDs at each

221   hour, and then subtract them from the total SCDs to obtain tropospheric SCDs (Eqs. (6) and (7)). In the

222   stratosphere, the geometric AMFs are essentially the same as the actual AMFs

223
$$SCD_{strat,h} = VCD_{strat,h} \times AMFgeo_h^{GEMS} \tag{6}$$

224
$$SCD_{trop,h}^{GEMS*} = SCD_{total,h}^{corrected} - SCD_{strat,h} \tag{7}$$
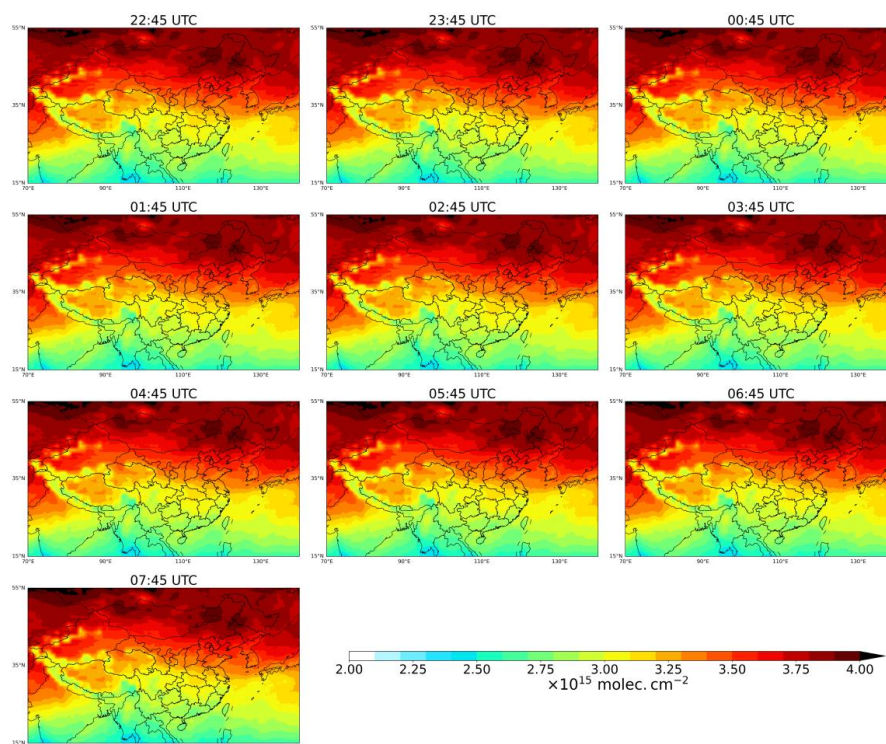
225

226   **Figure 3. Spatial distribution of POMINO-GEMS derived monthly mean stratospheric NO$_2$ VCDs at each**

227   **hour on a 0.05° × 0.05 °grid in June 2021.** Note the range of the color bar is $2.0 - 4.0 \times 10^{15}$ molec. cm^{-2}.

228   **2.1.5 Calculation of tropospheric AMFs**

229   For tropospheric AMF calculations (Figure 1), we use a parallelized LIDORT-driven AMFv6

230   package; this is similar to the one used in our previous POMINO products (Lin et al., 2014; Lin et al.,

231   2015; Liu et al., 2019) but with modifications to adapt to the geostationary observing characteristics and

232   high spatiotemporal resolution of GEMS. We take daily BRDF coefficients with a horizontal resolution

233   of 5 km from the MODIS MCD43C2.006 dataset (Lucht et al., 2000; Lin et al., 2014; Lin et al., 2015;

234 Liu et al., 2020) to account for the anisotropy of surface reflectance (Zhou et al., 2010). Hourly-varying

235 aerosol parameters, a priori NO_2 profiles as well as temperature and pressure profiles are interpolated

236 from nested GEOS-Chem (v9-02) results to a horizontal resolution of 2.5 km, using the Piecewise Cubic

237 Hermite Interpolating Polynomial (PCHIP) method. Furthermore, we deploy AOD observations from the

238 MODIS MYD04_L2 dataset (Lin et al., 2014; Lin et al., 2015; Liu et al., 2019; Liu et al., 2020) to

239 constrain model-simulated AOD on a monthly basis, and we use a self-constructed monthly

240 climatological dataset of aerosol extinction profiles based on CALIOP L2 data over 2007-2015 to

241 constrain modeled aerosol vertical profiles on a monthly climatology basis (Liu et al., 2019). We re-

242 retrieve cloud parameters based on O_2-O_2 SCDs and continuum reflectances from the official GEMS

243 v1.0 cloud product, using ancillary parameters consistent with those used in NO_2 AMF calculations.

244 Instead of relying on a look-up table (LUT), we conduct pixel-by-pixel radiative transfer calculations

245 with the parallelized AMFv6 package. The independent pixel approximation (IPA) is assumed for cloud-

246 contaminated pixels as in other algorithms. Finally, we use the AMF data to convert tropospheric NO_2

247 SCDs to VCDs.

248 Invalid pixels are filtered based on the following criteria. We exclude pixels with solar zenith angle

249 (SZA) or viewing zenith angle (VZA) greater than 80°, or with the ground covered by ice or snow. To

250 minimize cloud contamination, we exclude pixels with cloud radiance fractions (CRF) greater than 50%

251 in the POMINO-GEMS product.

252 **2.2 Estimation of surface NO_2 concentrations**

253 In order to validate satellite NO_2 products with surface concentration measurements from MEE, we

254 convert tropospheric NO_2 VCDs on a 0.05° × 0.05° grid to surface NO_2 mass concentrations using

255 GEOS-Chem simulated NO_2 vertical profiles and the box heights of the lowest model layer (Eq. (8)).

$$256 \qquad C_{surf} = VCD_{trop}^{SAT} \times R^{GC} \times \frac{M}{N \times H^{GC}} \times 2 \qquad (8)$$

257 In Eq. (8), C_{surf} represents the estimated surface NO_2 mass concentration in μg m^{-3}, VCD_{trop}^{SAT} the

258 satellite tropospheric VCD in molec. m^{-2}, R^{GC} the GEOS-Chem simulated ratio of NO_2 sub-column in

259 the lowest layer to the total column, M the NO_2 molar mass in μg mol^{-1}, N the Avogadro constant, and

260 H^{GC} the box height of the lowest layer in m. The thickness of the lowest layer of GEOS-Chem (about

261 130 m) is too large for the layer average NO_2 mass concentration to represent that near the ground (Liu

Atmospheric
Measurement
Techniques
Discussions

Open Access

EGU

262   et al., 2018); thus the derived concentration is multiplied by a factor of 2 to roughly account for the

263   vertical gradient from the height of ground instrument to the center of the model layer.

264   **2.3 Ground-based MAX-DOAS measurements**

265   We use ground-based MAX-DOAS measurements to validate the POMINO-GEMS and POMINO-

266   TROPOMI v1.2.2 NO_2 products (Figure S2). The types, geolocations and observation times of MAX-

267   DOAS stations are summarized in Table 1. Details of each site are described in supplement information

268   (SI).

269   **Table 1. MAX-DOAS measurements**

Site name	Type	Geolocation	Measurement time
Fudan University	Urban	121.52°E, 31.34°N	1 June – 31 August 2021
Xuzhou	Suburban	117.14°E, 34.22°N	1 June – 31 August 2021
Hefei	Suburban	117.16°E, 31.91°N	1 June – 30 June 2021
Nanhui	Suburban	121.80°E, 31.06°N	1 June – 31 August 2021
Chongming	Suburban	121.82°E, 31.50°N	1 June – 31 August 2021
Dianshan Lake	Suburban	120.98°E, 31.30°N	1 June – 31 August 2021
Xianghe	Suburban	116.96°E, 39.75°N	1 June – 31 August 2021
Fukue	Remote	128.68°E, 32.75°N	1 June – 31 August 2021
Cape Hedo	Remote	128.25°E, 26.87°N	1 June – 31 August 2021

270

271   To ensure sampling consistency in time, we average all valid MAX-DOAS measurements within

272   each observation period of GEMS (i.e., 30 minutes) for hourly comparison, and within ± 1.5 h of

273   TROPOMI overpass time for daily comparison. Following the procedure in previous studies (Lin et al.,

274   2014; Liu et al., 2020), we exclude all matched MAX-DOAS data for which the standard deviation

275   exceeds 20% of the mean value to minimize the influence of local events. To ensure sampling consistency

276   in space, we select valid satellite pixels within 5 km of MAX-DOAS sites and conduct spatial averaging.

277   The Grubbs statistical test is performed to exclude outliers in both MAX-DOAS and satellite data before

278   comparison.

279   **2.4 Ground-based MEE NO$_2$ measurements**

280   We use hourly surface NO$_2$ mass concentration measurements from the MEE air quality monitoring

281   network (https://quotsoft.net/air/). By 2021, more than 2000 MEE stations across China have been

282   established, providing hourly observations for NO$_2$ and five other air pollutants. Most stations are in

283   urban or suburban areas. We filter the MEE sites for comparison with satellite data using mean surface-

284   to-total ratios of NO$_2$ (R^{GC}) in June-July-August 2021 defined in section 2.2. The spatial distribution of

285   R^{GC} is shown in Figure S3a. Only MEE sites at the grid cells where the surface-to-total ratio is larger

286   than the 95th percentile across all grid cells within the GEMS domain (i.e., 0.12) are included; this results

287   in 855 valid MEE sites, as shown in Figure S3b.

288   To compare with satellite-derived surface NO$_2$ concentration data, we average over all valid MEE

289   sites in each $0.05° \times 0.05°$ grid cell to generate gridded MEE NO$_2$ data for each hour. To ensure sampling

290   consistency for each day, we average MEE observations for two consecutive hours to match GEMS

291   hourly observations – for example, we match the mean value of MEE NO$_2$ concentrations in 13:00–14:00

292   and 14:00–15:00 LST with the GEMS NO$_2$ in 13:45–14:15 LST. We also match MEE observations over

293   the period 13:00–14:00 LST with TROPOMI-derived surface NO$_2$.

294   **3. Results and discussion**

295   **3.1 POMINO-GEMS tropospheric NO$_2$ VCDs**

296   Figure 4 shows mean POMINO-GEMS tropospheric NO$_2$ VCDs at each hour on a $0.05° \times 0.05°$

297   grid in JJA 2021. High values of tropospheric NO$_2$ columns ($> 10 \times 10^{15}$ molec. cm^{-2}) are evident over

298   populous regions such as South Korea, central and eastern China, and northern India. Clear hotspot

299   signals reveal intense NOx emissions over city clusters such as Beijing-Tianjin-Hebei (BTH), Yangtze

300 River Delta (YRD), Pearl River Delta (PRD) and Seoul Metropolitan Area (SMA), as well as isolated

301 megacities such as Osaka and Nagoya in Japan, Chengdu and Urumqi in China, and New Delhi in India.

302 Tropospheric NO_2 VCDs are much lower ($< 1 \times 10^{15}$ molec. cm^{-2}) over most of western China and the

303 open ocean, due to low anthropogenic and natural emissions.
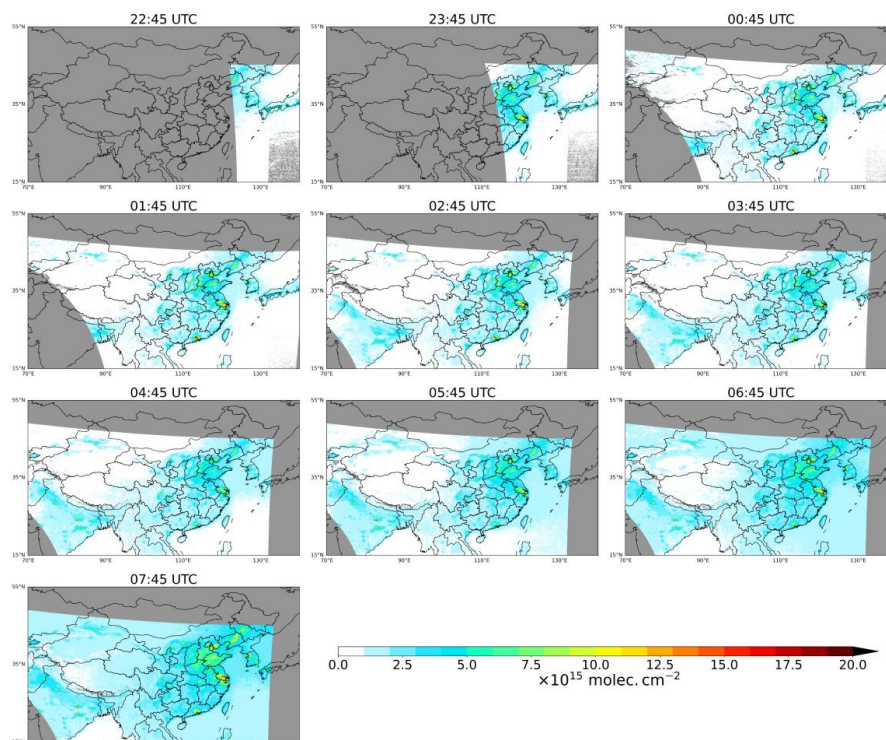
305 **Figure 4. Spatial distribution of POMINO-GEMS tropospheric NO_2 VCDs at each hour on a 0.05° × 0.05°**
306 **grid in JJA 2021.**

307 Figures 5 presents NO_2 VCDs in the morning, noon and afternoon in JJA 2021 for eastern China.

308 Data are averaged from 22:45–01:45 UTC (06:45–09:45 Beijing Time, BJT), 02:45–04:45 UTC (10:45–

309 12:45 BJT) and 05:45–07:45 UTC (13:45–15:45 BJT) to represent the morning, noon and afternoon,

310 respectively. In the morning (Figure 5a), there are clear city signals with high NO_2 values, reflecting

311 abundant NOx emissions from traffic. The spatial gradients of NO_2 from urban centers to outskirts are

312 very strong. However, these spatial gradients are greatly reduced in the noon and afternoon (Figure 5b

313 and c). For example, the differences of tropospheric NO_2 VCDs between the urban center of Xi'an

314 (108.93°N, 34.27°E) and its surrounding areas (within 50 km) are reduced from about 8×10^{15} molec.
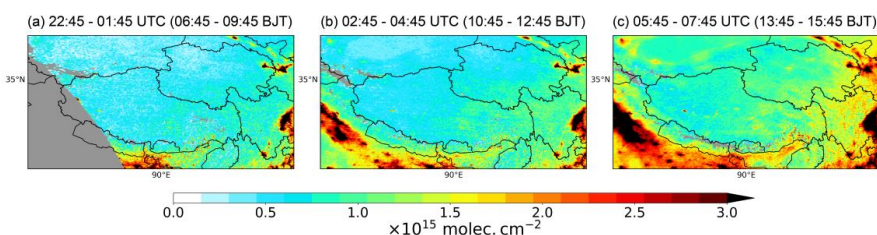
Atmospheric
Measurement
Techniques
Discussions

Open Access

EGU

315 cm^{-2} in the morning to about 4×10^{15} molec. cm^{-2} at noon, and then to below 2×10^{15} molec. cm^{-2} in the

316 afternoon. This is likely due to chemical loss of traffic-associated NO$_2$, increased emissions from other

317 sectors (e.g., industry), and/or enhanced horizontal transport smearing the gradient.
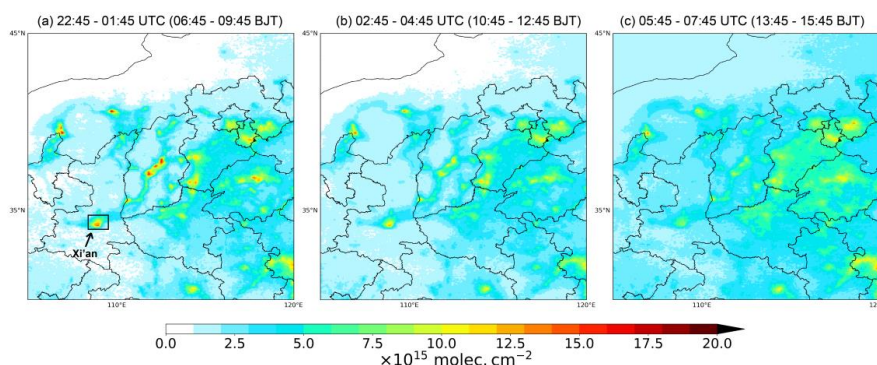
318

319 **Figure 5. Spatial distribution of three-hour-mean POMINO-GEMS tropospheric NO$_2$ VCDs on a 0.05° ×**

320 **0.05° grid over eastern China in the (a) morning, (b) noon and (c) afternoon in JJA 2021.**

321 Over western China with low tropospheric NO$_2$ VCDs (Figure 6), there is a roughly monotonic

322 increase of tropospheric NO$_2$ by about 1×10^{15} molec. cm^{-2} within daily GEMS observations. This

323 increase is likely dominated by biogenic NOx emissions that are sensitive to sunshine intensity and

324 surface temperature (Kong et al., 2022b; Weng et al., 2020). Future studies are needed to understand the

325 exact causes.

326

327 **Figure 6. Spatial distribution of three-hour-mean POMINO-GEMS tropospheric NO$_2$ VCDs on a 0.05° ×**

328 **0.05° grid over western China in JJA 2021. The local solar time in this region is 1-3 hours earlier than**

329 **Beijing Time.**

330 **3.2 Comparison with POMINO-TROPOMI v1.2.2 NO$_2$ product**

331 Figures 7a and b show the POMINO-GEMS and POMINO-TROPOMI v1.2.2 tropospheric NO$_2$

332 VCDs, respectively, on a 0.05° × 0.05 ° grid averaged over JJA 2021. Cloud screening is implemented

333 based on the CRFs from each product. To ensure temporal compatibility, matching between hourly

334   GEMS observations and the TROPOMI data at the closest observation time is done for each day. Overall,

335   POMINO-GEMS agrees well with POMINO-TROPOMI with a spatial correlation coefficient of 0.97, a

336   linear regression slope of 1.15 and a small positive normalized mean bias (NMB) of 3.6% (Figure 7c).
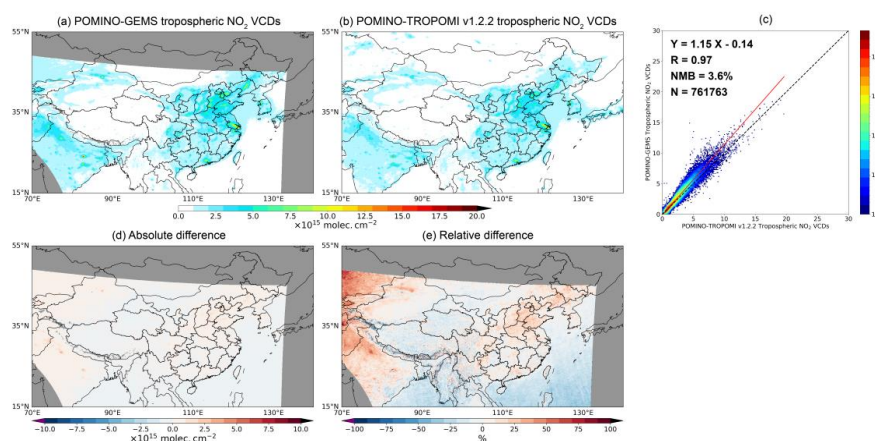

337

338   **Figure 7. Comparison between POMINO-GEMS and POMINO-TROPOMI tropospheric NO₂ VCDs.**
339   **Spatial distributions of (a) POMINO-GEMS and (b) POMINO-TROPOMI v1.2.2 tropospheric NO₂ VCDs**
340   **on a 0.05° × 0.05 °grid in JJA 2021. (c) Scatterplot for tropospheric NO₂ VCDs between these two products.**
341   **Colors represent the data density. Panels (d) and (e) are absolute and relative differences between**
342   **POMINO-GEMS and POMINO-TROPOMI v1.2.2, respectively.**

343   POMINO-GEMS VCDs are higher than those from POMINO-TROPOMI over eastern China and

344   smaller over the oceans (Figures 7d and e). These differences are mainly because POMINO-GEMS

345   AMFs are lower (higher) than POMINO-TROPOMI AMFs over polluted regions (ocean). POMINO-

346   GEMS explicitly employs CALIOP-corrected aerosol vertical profiles and re-calculates cloud fraction

347   and cloud pressure based on continuum reflectances and O_2-O_2 SCDs from GEMS observations. By

348   comparison, POMINO-TROPOMI v1.2.2 does not use CALIOP observations to constrain aerosol

349   vertical profiles; and it takes the FRESCO-wide cloud pressure data from TROPOMI PAL v2.3.1 NO₂

350   product and re-calculates cloud fraction at 440 nm. Constraint by CALIOP observations results in higher

351   aerosol-concentrated layer heights (Liu et al., 2019), which enhances the "screening" effect on the

352   absorption by NO₂ over polluted regions and leads to lower AMFs. Over remote areas where lightning

353   produced NO₂ is presented at altitudes higher than the aerosol-concentrated layer, higher aerosols tend

354   to enhance the "albedo" effect and lead to higher AMFs (Lin et al., 2015).

3.3 Validation with MAX-DOAS NO$_2$ VCD measurements

The scatterplot in Figure 8a compares POMINO-GEMS tropospheric NO$_2$ VCDs in JJA 2021 at all GEMS observation hours with matched MAX-DOAS measurements at nine sites. POMINO-GEMS correlates with MAX-DOAS ($R = 0.62$) with a small negative bias (NMB = −15.7%). The linear regression shows a slope of 0.47 and intercept of 3.37×10^{15} molec. cm^{-2}, reflecting underestimation of POMINO-GEMS tropospheric NO$_2$ VCDs on high-NO$_2$ days.
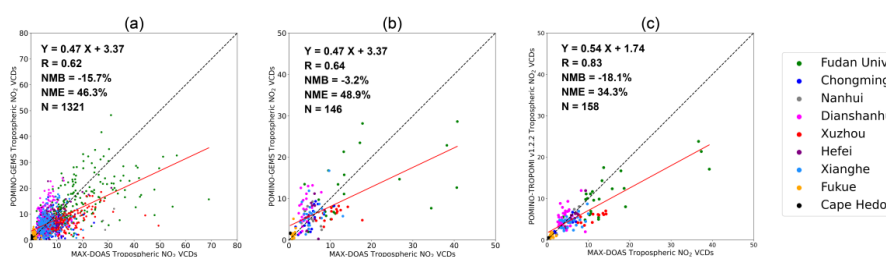

Figure 8. Evaluation of satellite NO$_2$ VCD data using MAX-DOAS measurements. (a) Scatterplot for tropospheric NO$_2$ VCDs ($\times 10^{15}$ molec. cm^{-2}) between MAX-DOAS and POMINO-GEMS at all GEMS observation hours in JJA 2021. Each data pair denotes an hour. (b-c) Scatterplots for tropospheric NO$_2$ VCDs ($\times 10^{15}$ molec. cm^{-2}) in JJA 2021 (b) between MAX-DOAS and POMINO-GEMS at 13:45 – 14:15 LST and (c) between MAX-DOAS and POMINO-TROPOMI v1.2.2. Each data pair denotes a day. Each MAX-DOAS stations are color-coded as indicated.

Figures 8b-c further use MAX-DOAS measurements to evaluate POMINO-GEMS and POMINO-TROPOMI v1.2.2 tropospheric NO$_2$ VCDs at the overpass time of TROPOMI. In Figure 8b, POMINO-GEMS data at 13:45–14:15 LST are used to match the overpass time of TROPOMI. POMINO-TROPOMI product is evaluated in the context of understanding the relative performance of POMINO-GEMS. Each data point represents a day. Figures 8b-c shows that the day-to-day variability of MAX-DOAS measurements is well captured by POMINO-TROPOMI v1.2.2 ($R = 0.83$), but less so by POMINO-GEMS ($R = 0.64$). Linear regression results show an underestimate of tropospheric NO$_2$ VCDs in POMINO-TROPOMI v1.2.2 product (NMB = −18.1%), as also found in previous studies (Liu et al., 2020). POMINO-GEMS exhibits a small bias (NMB = −3.2%), but station-dependent performance is apparent in the scatterplot of Figure 8b. At the two remote sites of Fukue and Cape Hedo with low NO$_2$, POMINO-GEMS tends to overestimate MAX-DOAS measurements. At the seven urban/suburban sites, the data pairs are more scattered and located both above and below the 1:1 line, resulting in a small NMB. Furthermore, the normalized mean error (NME) of POMINO-GEMS relative to MAX-DOAS measurements (46.3% at all observation hours and 48.9% at 13:45-14:45 LST) is higher than that of

382 POMINO-TROPOMI (34.3%), indicating that the uncertainty in POMINO-GEMS NO_2 is larger than

383 POMINO-TROPOMI.

384 Figure 9 also compares the diurnal variation of tropospheric NO_2 VCDs between POMINO-GEMS

385 and MAX-DOAS at eight MAX-DOAS stations. At each site, NO_2 values are averaged in JJA 2021 at

386 each hour for comparison, and the number of valid days at each hour is shown in Figure S4. The Cape

387 Hedo site is not included because there are few valid MAX-DOAS data points at each hour. Figures 9a-

388 g show that at the urban and suburban sites, MAX-DOAS NO_2 peaks in the mid-to-late morning, declines

389 towards the minimum values at noon, and then gradually increases in the afternoon. Strong correlation

390 of NO_2 diurnal variation between POMINO-GEMS and MAX-DOAS is found at Xuzhou ($R = 0.90$) and

391 Hefei ($R = 0.72$), although the correlation is much weaker at Fudan University ($R = 0.23$) and Nanhui (R

392 $= 0.12$). At Chongming, Xianghe and Dianshan Lake sites, POMINO-GEMS exhibits a maximum in the

393 late afternoon and a second maximum in the mid-morning (Figures 9e-g), a pattern which is poorly

394 correlated with MAX-DOAS ($R = -0.02$, -0.23 and -0.66, respectively). At Fukue, MAX-DOAS NO_2

395 shows a peak in the morning and then declines to low values around 1×10^{15} molec. cm^{-2}, but this diurnal

396 pattern is not captured by POMINO-GEMS. Overall, the mixed performance at these eight sites suggests

397 that more work is warranted to further improve the POMINO-GEMS retrieval algorithm.
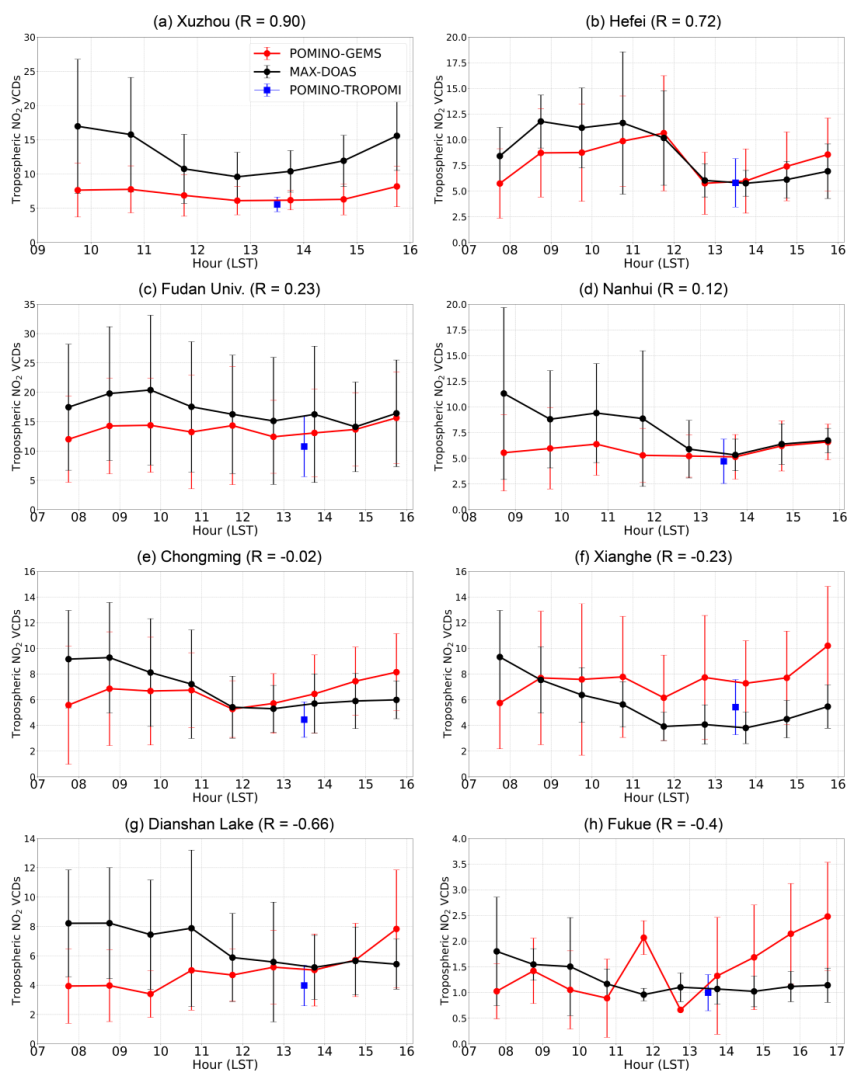
Figure 9. Diurnal variation of hourly tropospheric NO$_2$ VCDs (× 10^{15} molec. cm^{-2}) from MAX-DOAS and POMINO-GEMS at eight sites in JJA 2021. The error bars denote the standard deviation of MAX-DOAS and POMINO-GEMS NO$_2$ at each hour in JJA 2021, respectively. The temporal correlation coefficients are also shown. In each panel, the blue square with an error bar represents the mean value and standard deviation of POMINO-TROPOMI v1.2.2 NO$_2$ in JJA 2021.

3.4 Validation with surface NO$_2$ concentration measurements from MEE

The scatterplot in Figure 10a further compares surface NO$_2$ concentrations derived from POMINO-GEMS with MEE measurements at all hours. Here, each data pair represents a site and hour averaged over

407   all days in JJA 2021. POMINO-GEMS derived surface NO_2 concentrations show good agreement with

408   MEE measurements in terms of spatiotemporal correlation ($R = 0.76$) and bias (NMB = −24.1%). Despite

409   the overall underestimate, POMINO-GEMS derived surface NO_2 concentrations show overestimation at

410   some high-value situations, which mainly occur over the YRD region (Figure S5). These differences

411   reflect errors in POMINO-GEMS NO_2 VCDs, in the conversion from tropospheric VCDs to surface

412   concentrations, and/or in MEE measurements. In particular, the MEE measurements are contaminated

413   by oxidation products of NO_2 (e.g., HNO_3 and PANs) and tend to overestimate the actual concentrations

414   of NO_2 (Liu et al., 2018), with the extent of contamination more severe for more aged air.
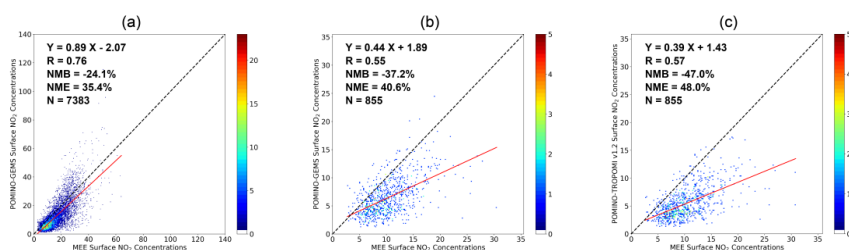
415

416   **Figure 10. Evaluation of satellite derived surface NO_2 concentrations using MEE measurements. (a)**

417   **Scatterplot for surface NO_2 concentrations (µg m⁻³) between MEE and POMINO-GEMS at all GEMS**

418   **observation hours averaged over JJA 2021. (b-c) Scatterplot for surface NO_2 concentrations in JJA 2021 (b)**

419   **between MEE and POMINO-GEMS at 13:45 – 14:15 LST, and (c) between MEE and POMINO-TROPOMI**

420   **v1.2.2. The color bar represents the data density.**

421   Figures 10b-c show validation results for satellite-derived surface NO_2 concentrations with MEE

422   measurements at 855 sites at the overpass time of TROPOMI (i.e., early afternoon). Here, each data pair

423   denotes a MEE site. POMINO-GEMS results at 13:45–14:15 LST are used to match the overpass time

424   of TROPOMI data. Overall, both satellite-based datasets show good spatial correlation with MEE

425   measurements, with correlation coefficients of 0.55 and 0.57, respectively. POMINO-GEMS exhibits

426   higher linear regression slope (0.44) with smaller NMB (−37.2%) and NME (40.6%). The values of

427   satellite data are lower than those from MEE measurements, in part because of the aforementioned

428   contamination issues in MEE data.

429   Figure 11 further examines the diurnal variation of surface NO_2 concentrations averaged over JJA

430   2021 and all sites. The MEE data show a smooth and monotonic decline from the early morning to the

431   early afternoon, with a slight increase beginning at 15:00 LST. This diurnal pattern differs from those

432   seen in MAX-DOAS VCD data (Figure 9), due to the difference in sampling size between MEE and

433   MAX-DOAS, as well as the vertical distribution of NO_2 that affects the relationship between surface and

434   columnar NO_2. POMINO-GEMS derived surface NO_2 concentrations show similar diurnal variations to

435   those from MEE ($R = 0.95$), although with a peak at 10:00 LST and a gradual increase beginning at 14:00

436   LST.

437
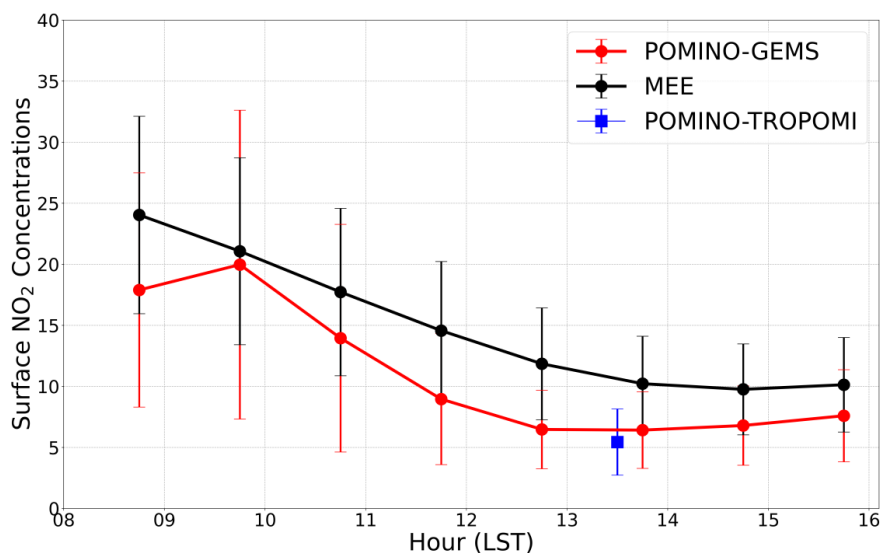
Figure 11. Diurnal variation of hourly surface NO_2 concentrations (µg m⁻³) for MEE and POMINO-GEMS

in JJA 2021. The error bars denote the standard deviation of MEE and POMINO-GEMS derived surface

NO_2 concentrations at each hour in JJA 2021, respectively. The blue square with an error bar represents the

mean value and standard deviation of POMINO-TROPOMI v1.2.2 derived surface NO_2 concentrations.

442   **3.5 Error estimates for POMINO-GEMS tropospheric NO_2 VCDs**

443   Total retrieval errors for POMINO-GEMS tropospheric NO_2 VCDs are compounded from the

444   calculations of total SCDs, stratospheric SCDs, and tropospheric AMFs. Spatial and temporal averaging

445   across GEMS pixels can greatly reduce the random errors but will not affect the systematic errors. Here,

446   we provide a preliminary estimate of retrieval errors.

447   As described in Section 2, we calculate hourly total SCDs based on the original GEMS SCD data

448   and daily TROPOMI-guided corrections. We tentatively estimate the error in our corrected total SCD

449   data to be 10%, which is the same as the TROPOMI total SCD error (Van Geffen et al., 2022a),

450   considering that we essentially adjust GEMS total SCDs to match TROPOMI values. In constructing the

451   stratospheric NO_2 SCDs, the stratospheric VCDs are taken from TROPOMI PAL v2.3.1, scaled based on

452   GEOS-Chem simulations to account for diurnal variation, and then applied with geometric AMFs. We

453   assign an error of 0.2×10^{15} molec. cm^{-2} (5%–10%) to our hourly stratospheric SCDs, the same as the

454   value for TROPOMI (Van Geffen et al., 2022a). As such, we assume no error contributions from the

455   GEOS-Chem-based scaling and geometric AMFs. As most of the errors in total SCDs are absorbed in

456   the calculation of stratospheric SCDs (Van Geffen et al., 2015), the errors in tropospheric SCDs should

457   be 0.2×10^{15} molec. cm^{-2} (5%–40%) at most.

458   Tropospheric AMF calculations are the dominant error source for retrieved tropospheric NO_2 VCDs

459   over polluted regions. According to Liu et al. (2020), the AMF errors caused by uncertainties in surface

460   reflectance and a priori NO_2 profiles are about 10% each, and errors induced by uncertainties in aerosol

461   parameters are about 10% in clean regions and 20% for heavily polluted situations. We further assume

462   that the O_2-O_2 cloud retrieval algorithm introduces another error at the 10% level to the NO_2 AMFs. The

463   overall AMF errors for POMINO-GEMS are estimated to be 20%–30%, as determined by adding these

464   errors in quadrature.

465   The overall uncertainty in POMINO-GEMS tropospheric NO_2 VCDs is estimated by adding in

466   quadrature the errors in tropospheric NO_2 SCDs and AMFs, when these errors are expressed in the

467   relative sense. For pixels over remote regions with low tropospheric NO_2 abundances, the overall

468   retrieval uncertainty is dominated by errors in tropospheric SCDs and can reach 0.2×10^{15} molec. cm^{-2}

469   (or 30%–50%). For pixels with abundant tropospheric NO_2, the uncertainty of retrieved tropospheric

470   VCDs is dominated by the AMF errors and is estimated to be about 25%–35%. The error magnitude is

471   supported by the NMB and NME values shown in the validation results against MAX-DOAS and MEE

472   data (Figure 8a, b and Figure 10a, b).

473   **4. Conclusions**

474   The GEMS instrument provides an unprecedented opportunity for air quality monitoring at a high

475   spatiotemporal resolution. Our POMINO-GEMS algorithm retrieves tropospheric NO_2 VCDs as a

476   research product. The algorithm first calculates hourly tropospheric NO_2 SCDs through fusion of total

477   NO_2 SCDs from GEMS v1.0 L2 NO_2 product, total and stratospheric NO_2 columns from TROPOMI PAL

478   v2.3.1 L2 NO_2 product, and stratospheric NO_2 diurnal variations from GEOS-Chem simulations. The

479   fusion approach reduces the high bias in total SCDs and removes the stripe-like patterns in the official

480   GEMS v1.0 product. Our algorithm then calculates tropospheric NO_2 AMFs to convert SCDs to VCDs.

481   A preliminary estimate of retrieval errors is also given.

482   Our initial POMINO-GEMS data for JJA 2021 shows high values of tropospheric NO_2 VCDs with

483   clear hotspots ($> 10 \times 10^{15}$ molec. cm^{-2}) over regions where anthropogenic emissions of NOx are

484   abundant. The spatial gradients of tropospheric NO_2 VCDs from urban centers to surrounding areas are

485   substantial in the morning due to traffic emissions, and gradients are much reduced at noon and in the

486   afternoon. By comparison, a roughly monotonic increase of tropospheric NO_2 VCDs from the morning

487   to the afternoon is observed over clean regions of western China, likely as a result of enhanced biogenic

488   emissions.

489   POMINO-GEMS tropospheric NO_2 VCDs agree with POMINO-TROPOMI v1.2.2 in terms of

490   spatial correlation (0.97) and NMB (3.6%). POMINO-GEMS is also comparable with ground-based

491   MAX-DOAS measurements at nine rural/suburban/urban sites with a small NMB (−15.7%), although

492   the correlations are modest ($R = 0.62$). Both the bias and correlation values are smaller than POMINO-

493   TROPOMI v1.2.2 (NMB = −18.1%, $R = 0.83$). POMINO-GEMS captures the diurnal variation of MAX-

494   DOAS NO_2 VCDs at the Xuzhou ($R = 0.90$) and Hefei ($R = 0.72$) sites but not at others, for reasons that

495   are not clear at present.

496   We also compare surface NO_2 concentrations derived from VCDs from POMINO-GEMS and

497   POMINO-TROPOMI v1.2.2 products against MEE measurements, taking advantage of the large number

498   of MEE sites. For 855 selected sites at all GEMS observation hours, POMINO-GEMS derived surface

499   NO_2 concentration data exhibit a small NMB (–24.1%). For these sites at TROPOMI overpass times,

500   POMINO-GEMS derived surface NO_2 concentrations show a smaller magnitude of NMB (−37.2%) than

501   POMINO-TROPOMI v1.2.2 (−47.0%). Excellent agreement in diurnal variation between POMINO-

502   GEMS derived and MEE NO_2 averaged over all sites is exhibited ($R = 0.95$).

503   Overall, our comprehensive validation process highlights the good performance of POMINO-

504   GEMS tropospheric NO_2 VCD product, both in magnitude and spatiotemporal variation. Currently, the

505   Environmental Satellite Center of South Korea is updating the NO_2 SCD data to v2.0. We will update

506   our POMINO-GEMS algorithm accordingly, once the updated official NO_2 product becomes available

507   to provide the necessary inputs for our research product.

508

509   *Data availability*. The POMINO-GEMS NO_2 data are available at the ACM group product website

510   (http://www.pku-atmos-acm.org/acmProduct.php/). The TROPOMI PAL v2.3.1 L2 product can be

Atmospheric
Measurement
Techniques
Discussions

511   downloaded from https://data-portal.s5p-pal.com. MEE surface NO$_2$ measurements can be downloaded

512   from https://quotsoft.net/air/. MAX-DOAS measurements can be provided upon requests to the

513   corresponding owners.

514

515   *Author contributions*. JL conceived this research. YZ and JL designed the algorithm and validation

516   process. YZ performed all calculations with additional code support from HK. YZ and JL wrote the paper.

517   RS provided LIDORT. JK, HL, JP and HH provided GEMS data. MV, QH, KQ, YC, YK, JX and PX

518   provided the MAX-DOAS measurements. HK helped process MEE measurements. LC and ML helped

519   analyze the validation results. All authors commented on the paper.

520

521   *Competing interests*. The authors declare that they have no conflicts of interest.

522

523   *Financial support*. This research has been supported by the National Natural Science Foundation of

524   China (grant no. 42075175) and the second Tibetan Plateau Scientific Expedition and Research Program

525   (grant no. 2019QZKK0604).

526

527   **References**

528   Beirle, S., Boersma, K. F., Platt, U., Lawrence, M. G., and Wagner, T.: Megacity Emissions and

529   Lifetimes of Nitrogen Oxides Probed from Space, Science, 333, 1737-1739, 10.1126/science.1207824,

530   2011.

531   Boersma, K. F., Eskes, H. J., and Brinksma, E. J.: Error analysis for tropospheric NO2retrieval from

532   space, Journal of Geophysical Research: Atmospheres, 109, n/a-n/a, 10.1029/2003jd003962, 2004.

533   Boersma, K. F., Eskes, H. J., Dirksen, R. J., van der A, R. J., Veefkind, J. P., Stammes, P., Huijnen,

534   V., Kleipool, Q. L., Sneep, M., Claas, J., Leitão, J., Richter, A., Zhou, Y., and Brunner, D.: An improved

535   tropospheric NO2 column retrieval algorithm for the Ozone Monitoring Instrument, Atmospheric

536   Measurement Techniques, 4, 1905-1928, 10.5194/amt-4-1905-2011, 2011.

537   Chen, L., Lin, J., Martin, R., Du, M., Weng, H., Kong, H., Ni, R., Meng, J., Zhang, Y., Zhang, L.,

538   and van Donkelaar, A.: Inequality in historical transboundary anthropogenic PM2.5 health impacts,

539   Science Bulletin, https://doi.org/10.1016/j.scib.2021.11.007, 2021.

23

540   Chen, L., Lin, J., Ni, R., Kong, H., Du, M., Yan, Y., Liu, M., Wang, J., Weng, H., Zhao, Y., Li, C.,

541   and Martin, R. V.: Historical transboundary ozone health impact linked to affluence, Environmental

542   Research Letters, 17, 104014, 10.1088/1748-9326/ac9009, 2022.

543   Cooper, M. J., Martin, R. V., Hammer, M. S., Levelt, P. F., Veefkind, P., Lamsal, L. N., Krotkov, N.

544   A., Brook, J. R., and Mclinden, C. A.: Global fine-scale changes in ambient NO2 during COVID-19

545   lockdowns, Nature, 601, 380-387, 10.1038/s41586-021-04229-0, 2022.

546   Crutzen, P. J.: The influence of nitrogen oxides on the atmospheric ozone content, Quarterly Journal

547   of the Royal Meteorological Society, 96, 320-325, 10.1002/qj.49709640815, 1970.

548   Cui, Y., Lin, J., Song, C., Liu, M., Yan, Y., Xu, Y., and Huang, B.: Rapid growth in nitrogen dioxide

549   pollution over Western China, 2005–2013, Atmos. Chem. Phys., 16, 6207-6221, 10.5194/acp-16-6207-

550   2016, 2016.

551   Eskes, H., Van Geffen, J., Sneep, M., Veefkind, P., Niemeier, S., and Zehner, C.: S5P Nitrogen

552   Dioxide v02.03.01 intermediate reproecessing on the S5P-PAL system: Readme file, 2021.

553   Gu, D., Wang, Y., Smeltzer, C., and Boersma, K. F.: Anthropogenic emissions of NOxover China:

554   Reconciling the difference of inverse modeling results using GOME-2 and OMI measurements, Journal

555   of Geophysical Research: Atmospheres, 119, 7732-7740, 10.1002/2014jd021644, 2014.

556   Hoek, G., Krishnan, R. M., Beelen, R., Peters, A., Ostro, B., Brunekreef, B., and Kaufman, J. D.:

557   Long-term air pollution exposure and cardio- respiratory mortality: a review, Environmental Health, 12,

558   43, 10.1186/1476-069X-12-43, 2013.

559   Kim, J., Jeong, U., Ahn, M.-H., Kim, J. H., Park, R. J., Lee, H., Song, C. H., Choi, Y.-S., Lee, K.-

560   H., Yoo, J.-M., Jeong, M.-J., Park, S. K., Lee, K.-M., Song, C.-K., Kim, S.-W., Kim, Y. J., Kim, S.-W.,

561   Kim, M., Go, S., Liu, X., Chance, K., Chan Miller, C., Al-Saadi, J., Veihelmann, B., Bhartia, P. K., Torres,

562   O., Abad, G. G., Haffner, D. P., Ko, D. H., Lee, S. H., Woo, J.-H., Chong, H., Park, S. S., Nicks, D., Choi,

563   W. J., Moon, K.-J., Cho, A., Yoon, J., Kim, S.-K., Hong, H., Lee, K., Lee, H., Lee, S., Choi, M., Veefkind,

564   P., Levelt, P. F., Edwards, D. P., Kang, M., Eo, M., Bak, J., Baek, K., Kwon, H.-A., Yang, J., Park, J.,

565   Han, K. M., Kim, B.-R., Shin, H.-W., Choi, H., Lee, E., Chong, J., Cha, Y., Koo, J.-H., Irie, H., Hayashida,

566   S., Kasai, Y., Kanaya, Y., Liu, C., Lin, J., Crawford, J. H., Carmichael, G. R., Newchurch, M. J., Lefer,

567   B. L., Herman, J. R., Swap, R. J., Lau, A. K. H., Kurosu, T. P., Jaross, G., Ahlers, B., Dobber, M., Mcelroy,

568   C. T., and Choi, Y.: New Era of Air Quality Monitoring from Space: Geostationary Environment

569   Monitoring Spectrometer (GEMS), Bulletin of the American Meteorological Society, 101, E1-E22,

570   10.1175/bams-d-18-0013.1, 2020.

571   Kong, H., Lin, J., Chen, L., Zhang, Y., Yan, Y., Liu, M., Ni, R., Liu, Z., and Weng, H.: Considerable

572   Unaccounted Local Sources of NOx Emissions in China Revealed from Satellite, Environmental Science

573   & Technology, 56, 7131-7142, 10.1021/acs.est.1c07723, 2022a.

574   Kong, H., Lin, J., Zhang, Y., Li, C., Xu, C., Shen, L., Liu, X., Yang, K., Su, H., and Xu, W.:

575   Unexpected high NOX emissions from lakes on Tibetan Plateau under rapid warming, 10.21203/rs.3.rs-

576   1980236/v1,   2022b.

577   Krotkov, N. A., McLinden, C. A., Li, C., Lamsal, L. N., Celarier, E. A., Marchenko, S. V., Swartz,

578   W. H., Bucsela, E. J., Joiner, J., Duncan, B. N., Boersma, K. F., Veefkind, J. P., Levelt, P. F., Fioletov, V.

579   E., Dickerson, R. R., He, H., Lu, Z., and Streets, D. G.: Aura OMI observations of regional SO2 and NO2

580   pollution changes from 2005 to 2015, Atmos. Chem. Phys., 16, 4605-4629, 10.5194/acp-16-4605-2016,

581   2016.

582   Lee, H., Park, J., and Hong, H.: Geostationary Environment Monitoring Spectrometer (GEMS)

583   Algorithm Theoretical Basis Document NO2 Retrieval Algorithm, 2020.

584   Lee, Y., Ahn, M. H., Kang, M., and Eo, M.: Spectral replacement using machine learning methods

585   for continuous mapping of the Geostationary Environment Monitoring Spectrometer (GEMS), Atmos.

586   Meas. Tech., 16, 153-168, 10.5194/amt-16-153-2023, 2023.

587   Lin, J. T. and McElroy, M. B.: Detection from space of a reduction in anthropogenic emissions of

588   nitrogen oxides during the Chinese economic downturn, Atmos. Chem. Phys., 11, 8171-8188,

589   10.5194/acp-11-8171-2011, 2011.

590   Lin, J. T., Liu, M. Y., Xin, J. Y., Boersma, K. F., Spurr, R., Martin, R., and Zhang, Q.: Influence of

591   aerosols and surface reflectance on satellite NO2 retrieval: seasonal and spatial characteristics and

592   implications for NOx emission constraints, Atmospheric Chemistry and Physics, 15, 11217-11241,

593   10.5194/acp-15-11217-2015, 2015.

594   Lin, J. T., Martin, R. V., Boersma, K. F., Sneep, M., Stammes, P., Spurr, R., Wang, P., Van

595   Roozendael, M., Clémer, K., and Irie, H.: Retrieving tropospheric nitrogen dioxide from the Ozone

596   Monitoring Instrument: effects of aerosols, surface reflectance anisotropy, and vertical profile of nitrogen

597   dioxide, Atmospheric Chemistry and Physics, 14, 1441-1461, 10.5194/acp-14-1441-2014, 2014.

Atmospheric
Measurement
Techniques
Discussions

598   Liu, M., Lin, J., Wang, Y., Sun, Y., Zheng, B., Shao, J., Chen, L., Zheng, Y., Chen, J., Fu, T. M., Yan,

599   Y., Zhang, Q., and Wu, Z.: Spatiotemporal variability of NO2 and PM2.5 over Eastern China:

600   observational and model analyses with a novel statistical method, Atmos. Chem. Phys., 18, 12933-12952,

601   10.5194/acp-18-12933-2018, 2018.

602   Liu, M., Lin, J., Kong, H., Boersma, K. F., Eskes, H., Kanaya, Y., He, Q., Tian, X., Qin, K., Xie, P.,

603   Spurr, R., Ni, R., Yan, Y., Weng, H., and Wang, J.: A new TROPOMI product for tropospheric NO2

604   columns over East Asia with explicit aerosol corrections, Atmos. Meas. Tech., 13, 4247-4259,

605   10.5194/amt-13-4247-2020, 2020.

606   Liu, M., Lin, J., Boersma, K. F., Pinardi, G., Wang, Y., Chimot, J., Wagner, T., Xie, P., Eskes, H.,

607   Van Roozendael, M., Hendrick, F., Wang, P., Wang, T., Yan, Y., Chen, L., and Ni, R.: Improved aerosol

608   correction for OMI tropospheric NO2 retrieval over East Asia: constraint from CALIOP aerosol vertical

609   profile, Atmospheric Measurement Techniques, 12, 1-21, 10.5194/amt-12-1-2019, 2019.

610   Lorente, A., Boersma, K. F., Stammes, P., Tilstra, L. G., and Muller, J. P.: The importance of surface

611   reflectance anisotropy for cloud and NO2 retrievals from GOME-2 and OMI, 2018.

612   Lorente, A., Boersma, K. F., Yu, H., Dorner, S., Hilboll, A., Richter, A., Liu, M., Lamsal, L. N.,

613   Barkley, M. P., and De Smedt, I.: Structural uncertainty in air mass factor calculation for NO2 and HCHO

614   satellite retrievals, Atmospheric Measurement Techniques, 10, 759-782, 2016.

615   Lucht, W., Schaaf, C. B., and Strahler, A. H.: An algorithm for the retrieval of albedo from space

616   using semiempirical BRDF models, IEEE Transactions on Geoscience & Remote Sensing, 38, 977-998,

617   2000.

618   Richter, A., Begoin, M., Hilboll, A., and Burrows, J. P.: An improved NO$_2$ retrieval

619   for the GOME-2 satellite instrument, Atmospheric Measurement Techniques, 4, 1147-1159,

620   10.5194/amt-4-1147-2011, 2011.

621   Richter, A., Burrows, J. P., Nüß, H., Granier, C., and Niemeier, U.: Increase in tropospheric nitrogen

622   dioxide over China observed from space, Nature, 437, 129-132, 10.1038/nature04092, 2005.

623   Shindell, D. T., Faluvegi, G., Koch, D. M., Schmidt, G. A., Unger, N., and Bauer, S. E.: Improved

624   Attribution of Climate Forcing to Emissions, Science, 326, 716-718, 10.1126/science.1174760, 2009.

625   van der A, R. J., Mijling, B., Ding, J., Koukouli, M. E., Liu, F., Li, Q., Mao, H., and Theys, N.:

626   Cleaning up the air: effectiveness of air quality policy for SO2 and NOx emissions in China, Atmos.

Atmospheric
Measurement
Techniques
Discussions

627   Chem. Phys., 17, 1775-1789, 10.5194/acp-17-1775-2017, 2017.

628   Van Geffen, J., Eskes, H., Boersma, K. F., and Veefkind, P.: TROPOMI ATBD of the total and
629   tropospheric NO2 data products, 2022a.

630   Van Geffen, J., Boersma, K. F., Eskes, H., Sneep, M., Ter Linden, M., Zara, M., and Veefkind, J. P.:
631   S5P TROPOMI NO_2 slant column retrieval: method, stability, uncertainties and
632   comparisons with OMI, Atmospheric Measurement Techniques, 13, 1315-1335, 10.5194/amt-13-1315-
633   2020, 2020.

634   Van Geffen, J., Eskes, H., Compernolle, S., Pinardi, G., Verhoelst, T., Lambert, J.-C., Sneep, M.,
635   Ter Linden, M., Ludewig, A., Boersma, K. F., and Veefkind, J. P.: Sentinel-5P TROPOMI
636   NO_2 retrieval: impact of version v2.2 improvements and comparisons with OMI and
637   ground-based data, Atmospheric Measurement Techniques, 15, 2037-2060, 10.5194/amt-15-2037-2022,
638   2022b.

639   van Geffen, J. H. G. M., Boersma, K. F., Van Roozendael, M., Hendrick, F., Mahieu, E., De Smedt,
640   I., Sneep, M., and Veefkind, J. P.: Improved spectral fitting of nitrogen dioxide from OMI in the 405–
641   465 nm window, Atmos. Meas. Tech., 8, 1685-1699, 10.5194/amt-8-1685-2015, 2015.

642   Vasilkov, A., Krotkov, N., Yang, E. S., Lamsal, L., Joiner, J., Castellanos, P., Fasnacht, Z., and Spurr,
643   R.: Explicit and consistent aerosol correction for visible wavelength satellite cloud and nitrogen dioxide
644   retrievals based on optical properties from a global aerosol analysis, Atmos. Meas. Tech., 14, 2857-2871,
645   10.5194/amt-14-2857-2021, 2021.

646   Vasilkov, A. P., Qin, W., Krotkov, N. A., Lamsal, L. N., Spurr, R., Haffner, D. P., Joiner, J., Yang,
647   E., and Marchenko, S.: Accounting for the Effects of Surface BRDF on Satellite Cloud and Trace-Gas
648   Retrievals: A New Approach Based on Geometry-Dependent Lambertian-Equivalent Reflectivity
649   Applied to OMI Algorithms, Atmospheric Measurement Techniques, 10, 333-349, 2016.

650   Wei, J., Liu, S., Li, Z., Liu, C., Qin, K., Liu, X., Pinker, R. T., Dickerson, R. R., Lin, J., Boersma,
651   K. F., Sun, L., Li, R., Xue, W., Cui, Y., Zhang, C., and Wang, J.: Ground-Level NO_2
652   Surveillance from Space Across China for High Resolution Using Interpretable Spatiotemporally
653   Weighted Artificial Intelligence, Environmental Science & Technology, 56, 9988-9998,
654   10.1021/acs.est.2c03834, 2022.

655   Weng, H., Lin, J., Martin, R., Millet, D. B., Jaeglé, L., Ridley, D., Keller, C., Li, C., Du, M., and

656   Meng, J.: Global high-resolution emissions of soil NOx, sea salt aerosols, and biogenic volatile organic

657   compounds, Scientific Data, 7, 148, 10.1038/s41597-020-0488-5, 2020.

658   Zhang, Y., Lin, J., Liu, M., Kong, H., Chen, L., Weng, H., and Li, C.: High-resolution Tropospheric

659   NO2 Retrieval over Asia based on OMI POMINO v2.1 and Quantitative comparison with other products,

660   National Remote Sensing Bulletin, 10.11834/jrs.20221413, 2022.

661   Zhou, Y., Brunner, D., Spurr, R. J. D., Boersma, K. F., Sneep, M., Popp, C., and Buchmann, B.:

662   Accounting for surface reflectance anisotropy in satellite retrievals of tropospheric NO2, Atmospheric

663   Measurement Techniques, 3, 1185-1203, 2010.

664